Greenhouse gases modulate the strength of millennial-scale subtropical rainfall, consistent with future predictions

Fei Guo[1,2,3*], Steven C. Clemens[3,*], Yuming Liu[2,4], Ting Wang[2,4], Huimin Fan[2], Xingxing Liu[2],

Youbin Sun[2,5,6]

[1]Institute of Marine Science and Technology, Shandong University, Qingdao 266237, China

[2]State Key Laboratory of Loess and Quaternary Geology, Institute of Earth Environment, Chinese Academy of Sciences, Xian 710061, China

[3]Department of Earth, Environmental, and Planetary Sciences, Brown University, Providence, RI 02912-1846, USA

[4]University of Chinese Academy of Sciences, Beijing 100049, China

[5]Institute of Global Environmental Change, Xi'an Jiaotong University, Xi'an 710061, China

[6]Open Studio for Oceanic-Continental Climate and Environment Changes, Pilot National Laboratory for Marine Science and Technology (Qingdao), Qingdao 266200, China

Corresponding author: Fei Guo (guofei@ieecas.cn) and Steven C. Clemens (steven_clemens@brown.edu)

Highlights

The new precipitation-sensitive proxy (Ca/Ti) shows persistent millennial-scale East Asian summer monsoon changes over past 650 ka;

The magnitude of millennial-scale variability is modulated by AMOC at the eccentricity and precession bands.

Increasing GHG and strong insolation lead to more frequent occurrence of extreme rainfall, consistent with model results.

Abstract: Millennial-scale East Asian monsoon variability is closely associated with natural hazards through long-term variability in flood and drought cycles. Therefore, exploring what drives the millennial-scale variability is of significant importance for future prediction of extreme climates. Here we present a new East Asian summer monsoon (EASM) rainfall reconstruction from the northwest Chinese Loess Plateau (CLP) spanning the past 650 ka. The magnitude of millennial-scale variability (MMV) in EASM rainfall is linked to ice volume and greenhouse gas (GHG) at the 100-kyr eccentricity band and to GHG and summer insolation at the precession band. At the glacial-interglacial time scale, gradual changes in CO_2 during intermediate glaciations leads to increased variability in North Atlantic stratification and Atlantic meridional overturning circulation, propagating abrupt climate changes into East Asia via the westerlies. Within the 100-kyr cycle, precession variability further enhances the response, showing that stronger insolation and increased atmospheric GHG cause increases in the MMV of EASM rainfall. These findings indicate increased extreme precipitation events under future warming scenarios, consistent with model results.

Key words: EASM rainfall; Millennial-scale variability; GHG modulation; Insolation forcing

1. Introduction

Chinese loess is a unique terrestrial archive that can well document East Asian monsoon (EAM) variability at tectonic to millennial timescales (Porter and An, 1995; An, 2000). High-resolution loess records have revealed persistent millennial-scale (1-10 kyr periodicity) EAM fluctuations spanning the last several glacial cycles (Guo et al., 1996; Sun et al., 2012, 2021a,b; Guo et al., 2021), which are dynamically linked with high-latitude abrupt changes in the

48 north Atlantic including Heinrich (H) (Heinrich, 1988) and Dansgaard-Oeschger (DO) events

49 (Dansgaard et al., 1993). This millennial-scale monsoon variability is superimposed on

50 glacial-interglacial variations (Ding et al., 1999; Clemens et al., 2018). Abrupt summer monsoon

51 changes are closely linked to natural hazards such as flood and drought events (Huang et al., 2007),

52 since the summer monsoon plays a leading role in transporting water vapor from low-latitude

53 oceans to middle/high-latitude continents of the Northern Hemisphere (Liu et al., 2013; An et al.,

54 2015). Abrupt rainfall events associated with short-term summer monsoon variations strongly

55 influence agriculture, food production, water supply and social economic development (Huang et

56 al., 2007; Cook et al., 2010; Li et al., 2017). However, how these flood/drought events are affected

57 by both natural and anthropogenic factors remains poorly constrained. Understanding the

58 mechanisms that modulate the magnitude of millennial-scale variability (MMV) is of critical

59 importance for the scientific community as well as policy makers. Here we use the term

60 "modulate" in the context of lower-frequency components of the climate system influencing or

61 determining the amplitude of a higher-frequency components.

62 A number of well-dated, high-resolution speleothem $\delta^{18}O$ records have been developed in

63 recent years (Wang et al., 2008; Cheng et al., 2016), providing the opportunity to examine the

64 underlying relationship(s) between the MMV and potential longer-term (orbital-scale) modulators.

65 Cheng et al., (2016) hypothesized, on the basis of an East Asian composite speleothem $\delta^{18}O$

66 record ($\delta^{18}Osp$), that periods of maximum Northern Hemisphere summer insolation correspond to

67 weaker millennial-scale variability. Subsequently, however, Thirumalai et al (2020) showed that

68 precession does not modulate the MMV of $\delta^{18}Osp$ and postulated that it is, instead, modulated by

69 internal processes related to the cryosphere. This work also raised the possibility that $\delta^{18}Osp$ is

70   decoupled from regional Asian monsoon rainfall over millennial timescales (Zhang et al., 2018).

71   The latest research suggests that the MMV through the Pleistocene is influenced by both glacial

72   boundary condition and orbital configurations (Sun et al., 2021b). As such, two important

73   outstanding questions remain; is there a reliable proxy for East Asian summer monsoon (EASM)

74   rainfall at the millennial timescale and what factors modulate the MMV thereof?

75   Due to weak pedogenesis and high sedimentation rates, millennial-scale oscillations are well

76   preserved in the northwestern Chinese Loess Plateau (CLP) over the past glacial cycles (Sun et al.,

77   2021a;). The Linxia profile is well-suited for reconstructing rapid monsoon changes because it is

78   located in monsoon frontal zone and sensitive to high- and low-latitude climate variability (Guo et

79   al., 2021). To address the above questions, we have generated a high-resolution summer monsoon

80   proxy (Ca/Ti) from Linxia on the western CLP (Fig. 1). The Ca/Ti ratio is a precipitation-sensitive

81   proxy linked to summer monsoon rainfall (Guo et al., 2021). Low values of Ca/Ti indicate

82   stronger Ca leaching associated with intensified summer rainfall. The new precipitation proxy

83   (Ca/Ti) and $\delta^{18}Osp$ are evaluated to elucidate the modulating drivers of these two proxy records.

84   As discussed in the Results section, we find that the MMV of Ca/Ti is mainly modulated by ice

85   volume and greenhouse gases (GHG) at the eccentricity band. Both GHG and summer insolation

86   modulate the MMV of Ca/Ti at the precession band but not that of $\delta^{18}Osp$; $\delta^{18}Osp$ MMV is

87   modulated by winter insolation at the eccentricity and obliquity bands. The interpretations of these

88   results are presented in the Discussion section.

89   **2. Materials and Methods**

90   **2.1 Sampling and measurements**

91   The Linxia (LX; 103.63°E, 35.15°N, 2,200 m a.s.l.) loess record is located in the western edge

92   of the CLP (Fig. 1). At present, mean annual temperature and precipitation in this region are about

93   8.1°C and 484 mm, respectively, with ~80% of the annual precipitation falling during the summer

94   season (May to September). The 203.8 m-long core A (LXA) consists of 185 m of eolian

95   loess-paleosol sequences, underlain by 17 m of fluvial loess and 1.8 m of sandy gravel layers. The

96   72 m-long core B (LXB) and a 7 m pit were excavated in 2017. Powder samples were collected at

97   2 cm intervals for analyzing mean grain size (MGS) with the resolution ranging 10~200 yr/cm. As

98   well, 2-cm resolution samples were dried at 40°C overnight and ground to 200 mesh size (about

99   <75 μm) with an agate mortar and pestle, and then pressed into a plastic sheet (4 cm × 4 cm × 0.3

100   cm), creating a flat and homogeneous slide. The plastic slides were then placed on a wood pallet

101   for XRF scanning to obtain elemental intensities (Guo et al., 2021).

102   **2.2 Age model and evaluations of age uncertainties**

103   The chronological framework for Chinese loess-paleosol sequences is widely constructed by

104   matching grain-size to benthic LR04 δ^{18}O stack (Porter and An, 1995; Hao et al., 2012; Sun et al.,

105   2021a). A similar approach utilizes correlation to speleothem δ^{18}O in recent years (Beck et al.,

106   2018; Sun et al., 2021a; Zhang et al., 2022). The age model of Linxia profile is generated by

107   synchronizing Chinese loess and speleothem δ^{18}O records back to 650 ka (Sun et al., 2021a).

108   Detailed information of loess/paleosol boundaries is showed in Fig. 2. The first set of control

109   points tie the loess/paleosol boundaries S_6 to S_0 to the timing of the glacial terminations/inceptions

110   in speleothem δ^{18}O (Cheng et al., 2016). The second and third sets of age control points tie the

111   timing of precessional transition boundaries and abrupt cooling events in the MGS record to those

112   in speleothem δ^{18}O (Fig. 2b), based on the assumption that the East Asian summer and winter

113   monsoon co-vary at orbital timescales, and millennial-scale abrupt events are synchronous in the

114 northern hemisphere (Hemming et al., 2004; Sun et al., 2012; Clemens et al., 2018). The tie points

115 are shown in Fig. 2b.

116   The composite speleothem $\delta^{18}O$ record is well resolved by absolute U-Th dating and applied as

117 the target for regional synchronization. The errors are less than 2 kyr for the last 450 ka and

118 increase to 4-8 kyr before 450 ka (Cheng et al., 2019). The MGS record yields good correlation

119 between loess/paleosol boundaries and glacial/interglacial transitions of LR04 $\delta^{18}O$. The age

120 differences of most glacial terminations are around 2-4 kyr (Fig. 2b, Sun et al., 2021a). The

121 speleothem $\delta^{18}O$ synchronized age model is compared with benthic $\delta^{18}O$ age model to evaluate the

122 influence of age uncertainties on the wavelet coherence analysis. The small differences in the two

123 age models (correlation to marine $\delta^{18}O$ and to speleothem $\delta^{18}O$) make little difference in the MMV

124 and associated wavelet coherence (WTC). This is because tie points are separated by 20-30 kyrs

125 and the small differences in the tie-points among the two age models has insignificant influence

126 on the amplitude (MMV) of millennial-scale peaks. Only minor differences in the MMV WTC

127 phase are observed at the obliquity (450-550 ka) and precession bands (100-200 ka). (Compare

128 Fig. S1 with Fig. 4).

129 **2.3 Spectrum and wavelet coherence analyses**

130   In order to estimate the MMV, loess Ca/Ti and $\delta^{18}O_{sp}$ are linear interpolated at 0.1 kyr interval.

131 The WTC results remain unchanged unless the cutoff threshold is reduced to to 6 kyr or increased

132 it to 12 kyr; then original time series are filtered using a Butterworth filter at a cutoff threshold of

133 10 kyr (e.g. Ca/Ti-hi-10kyr). The moving standard deviation of millennial-scale variability is

134 calculated to ascertain the orbitally-related modulation and its association with internal and

135 external forcing using 2 kyr sliding window (calculation method follows Thirumalai et al., 2020).

136   The spectra of all proxies were calculated using the Lomb-Scargle periodogram

137   (https://exoplanetarchive.ipac.caltech.edu/cgi-bin/Pgram/nph-pgram), which has the advantage of

138   analyzing discontinuous time series and removal of spurious spectral characteristics (VanderPlas,

139   2018).

140   Normalized and combined orbital parameters eccentricity, tilt, and negative precession (ETP),

141   GHG, insolation, and benthic $\delta^{18}O$ were evaluated by WTC to extract maximal phase and

142   amplitude correlations with astronomical, ice volume and greenhouse gases forcing over the past

143   650 ka. WTC between time series was performed in a Monte Carlo framework (n = 1, 000)

144   following Grinsted et al., (2004). The WTC evaluates the time evolution of coherence between

145   two time series across a range of frequency bands (independent of the power). The black arrows in

146   the figures represent the phase relationship between the two time sequences with rightward,

147   upward and downward arrows indicating in-phase, leading and lagging phase, respectively. The

148   colour scale indicates the amplitude correlations between the two datasets.

149   In this paper, the parameter ΔRF_{GHG} is a measure of GHG radiative forcing. ΔRF_{GHG} is

150   reconstructed by referencing the content of EPICA ice core greenhouse gases to the modern value.

151   ΔRF_{GHG} is defined as the difference between a certain past GHG level ($[CO_2]$ and $[CH_4]$) and the

152   pre-industrial greenhouse gas level ($[CO_2]_0 = 280$ ppm, $[CH_4]_0 = 700$ ppb) (Ramaswamy et al.,

153   2001). While CH_4 contributes <5%, we calculated the ΔRF_{GHG} using both CO_2 and CH_4. The

154   equation used to determine ΔRF_{GHG} is as follows (Lo et al., 2017):

155    $\Delta RF_{GHG} = \Delta RF_{CO2} + \Delta RF_{CH4}$

156    $= 4.841 \ln([CO_2]/[CO_2]_0) + 0.0906(\sqrt{[CO_2]} - \sqrt{[CO_2]_0}) + 0.036 \ln(\sqrt{[CH_4]} - \sqrt{[CH_4]_0})$

157   **3. Results**

158   The MGS reflects grain-size sorting and is very sensitive to winter monsoon variations (Porter

159   and An, 1995; Sun et al., 2006) with coarser particle size during the glacials. The Ca/Ti ratio

160   reflects precipitation-induced leaching intensity linked to summer monsoon rainfall (Guo et al.,

161   2021), with relatively low values during the interglacials. The high resolution $\delta^{18}O$ of

162   Sanbao-Hulu speleothem is an indicator of EASM changes at orbital to millennial timescales

163   (Cheng et al., 2016). The MGS and Ca/Ti exhibit distinct glacial-interglacial and precessional

164   variations over the last 650 ka as seen in LR04 $\delta^{18}O$ (Lisiecki and Raymo, 2005) and speleothem

165    $\delta^{18}O$ (Cheng et al., 2016), respectively (Fig. 2b).

166   Both Ca/Ti and $\delta^{18}O_{sp}$ records show clear millennial-scale fluctuations overlaying orbital-scale

167   variations. The high frequency millennial signals were persistent over the last 650 ka, but the

168   amplitude varies from proxy to proxy (Fig. 3a and S2a). Spectral analysis of the raw records and

169   MMV for loess and speleothem records display variable associations with eccentricity- (~100 kyr),

170   obliquity- (~41 kyr), and precession-scale (~23 and ~19 kyr) over the past 650 ka. Loess Ca/Ti

171   variance is mainly concentrated in obliquity with lesser variance in the eccentricity and precession

172   bands (Fig. 3b), indicating prominent ice volume (eccentricity and obliquity) and isolation

173   (precession) forcing. The speleothem $\delta^{18}O$ shows predominant precession-scale variance (Fig. S2b)

174   suggesting strong links to insolation forcing (Cheng et al., 2016). These results indicate ice

175   volume and insolation play dominant roles in driving changes in loess Ca/Ti and speleothem $\delta^{18}O$,

176   respectively (Cheng et al., 2016; Sun et al., 2021a).

177   Millennial-scale fluctuations co-exist with long-term orbital- and ice-volume variability. We

178   seek to assess the potential linkages among them and in particular, the extent to which MMV is

179   modulated by these longer-term orbital and internal climate parameters. The spectrum of Ca/Ti

180   MMV shows dominant eccentricity with less strong precession and weak obliquity variance (Fig.

181   3d). The spectrum of $\delta^{18}Osp$ MMV has a small peak near 100 kyr and an offset 41 kyr peak with

182   little to no variance at the 23 kyr period (Fig. S2d). Thus, while both proxies are similarly

183   modulated at the 100-kyr period (i.e. larger MMV during glacial intervals relative to interglacial

184   times), the MMV modulation is variable for the two proxies at other orbital bands.

185   As with the spectral differences in the raw records, the MMV spectra also implies different

186   MMV modulating drivers, potentially associated with insolation, ice volume, and/or GHG

187   (Thirumalai et al., 2020). How do internal and external drivers interact with each other and

188   modulate the MMV of these records at the orbital timescale? We performed wavelet coherence

189   and phase analyses of both MMV records relative to ETP, ice volume, ΔRF_{GHG}, summer insolation,

190   and winter insolation to identify which variables might modulate the MMV of these EASM

191   records. The MMV in Ca/Ti is strongly coherent with ice volume and GHG at the 100-kyr

192   eccentricity band and with GHG and summer insolation at the 23-kyr precession band (Fig. 4c, d,

193   g). $\delta^{18}Osp$ MMV is most strongly coherent with GHG and ice volume at the 100-kyr band and

194   with winter insolation at the eccentricity and obliquity bands (Fig. S3c, d, g).

195   **4. Discussion**

196   **4.1 Orbital-scale modulation factors for MMV of the EASM**

197   Geological records and modeling results indicate that high latitude ice volume or ice sheet

198   topography play important roles in triggering abrupt climate changes (Broecker et al.,1994; Clark

199   et al., 2001). In particular, abrupt climate changes are highly sensitive to ice volume variations; ice

200   sheets are widely hypothesized to motivate and amplify these high frequency signals within a

201   constrained benthic oxygen isotope-"ice volume threshold" between 3.5 and 4.5‰ (McManus et

al., 1999; Bailey et al., 2010; Naffs et al., 2013; Zhang et al., 2014). Wavelet coherence between the MMV of loess Ca/Ti, speleothem $\delta^{18}O$ and the global benthic $\delta^{18}O$ stack show excellent coherence and near-zero phase with ice volume at the 100-kyr band (Fig. 4e, g and S3e, g). This in-phase variation demonstrates that EASM MMV primarily follows the glacial-interglacial rhythm of ice volume variations, enlarged during glacial times and dampened during interglacial times. However, coherence of the MMV for these two proxies with the benthic $\delta^{18}O$ stack is relatively weak and variable at the 41-kyr band ($\delta^{18}Osp$; Fig. S3e, g) and 23-kyr band (Ca/Ti; Fig. 4e, g). These relationships demonstrate that ice volume directly modulates the MMV of the EASM, predominantly at the 100-kyr band, with high ice volume corresponding to larger MMV.

GHG concentration is another potential driver of abrupt climate changes (Alvarez-Solas et al., 2011; Zhang et al., 2017). Wavelet results between the MMV of loess Ca/Ti, speleothem $\delta^{18}O$ and the record of GHG RF show excellent coherence and ~180° phase at the 100-kyr eccentricity band (Fig. 4b, d and S3b, d), indicating strong MMV at times of low GHG. Given the coupled nature of global ice-volume and atmospheric GHG, it is suggested that during the late Pleistocene glacial-interglacial cycles, these two factors can amplify the MMV of the EASM as recorded by Ca/Ti and speleothem $\delta^{18}O$ during times of high ice volume and low GHG concentration. However, this is not the case for the precession band. MMV of loess Ca/Ti displays discrete intervals of high-coherence and near-zero phase with GHG RF at the precession band (Fig. 4b, d), which is not the case for speleothem $\delta^{18}O$ (Fig. S3b, d). Thus, GHG RF does play a role in modulating Ca/Ti MMV but not that of $\delta^{18}Osp$ at the precession band, indicating a difference in the millennial-scale response of these two proxies. We investigate this further by assessing the response to local insolation forcing.

224   The MMV of Ca/Ti show discontinuous relatively weak coherence with 35°N summer

225   insolation at the precession band with even weaker coherence at the 41-kyr band (Fig. 4a, c), and

226   relative strong mudulation of the summer insolation compared to that of GHG at the precession

227   band (Fig. 4b, d). In contrast, the MMV of $\delta^{18}Osp$ displays high coherence and zero phase with

228   35°N winter insolation at 100 kyr period, relatively weaker coherence, with a lagging phase, at the

229   41 kyr band, and negligible coherence at the 23-ky band (Fig. S3a, c). These results indicate that

230   the MMV of speleothem $\delta^{18}O$ is modulated by local winter insolation, opposite to the hypothesis

231   calling on north hemisphere summer insolation (Cheng et al., 2016).

232   **4.2 Mechanisms and implication for modulation of EASM MMV**

233   At the glacial-interglacial timescale, the MMV is amplified under the glacial boundary

234   conditions. This indicates dynamic linkages with high latitude North Atlantic Heinrich and DO

235   events (Cheng et al., 2016; Sun et al., 2012, 2021a, b). Heinrich and DO variability are linked to

236   Northern Hemisphere ice sheet (NHIS) perturbations via its influence on fresh-water flux into the

237   North Atlantic Ocean and consequent Atlantic meridional overturning circulation (AMOC)

238   changes (McManus et al., 1999; Hemming, 2004; Naffs et al., 2013). At times of intermediate ice

239   sheet volume, minor changes in NHIS height and atmospheric CO_2 concentrations can trigger the

240   rapid climate transitions (Zhang et al., 2014, 2017). Altering the height of NHIS leads to changes

241   in the gyre circulation and sea-ice coverage by shifting the northern westerlies (Zhang et al., 2014).

242   The maximum westerly wind stress shifts northwards associated with gradual increase of the

243   Northern Hemisphere ice volume. The northward westerly, in turn, encourages the EASM rain belt

244   to move northward (He et al., 2021) and results in increases in the MMV of EASM rainfall

245   (especially northern China).

246   In addition, CO_2 acts as an internal feedback agent to AMOC changes (Barker et al., 2016).

247   Under intermediate glacial condition, when the AMOC reaches a regime of bi-stability, rising CO_2

248   during Heinrich Stadial cold events can trigger abrupt transitions to warm conditions. Decreasing

249   CO_2 during warm events leads to abrupt cooling transitions (Zhang et al., 2017). Therefore, CO_2

250   generally provides a negative feedback on MMV of EASM rainfall. During interglacial times

251   decreasing ice volume, accompanied by reduced sea ice and more frequent freshwater perturbation,

252   is correlated with lower frequency and smaller amplitude variability in abrupt climate events. The

253   co-evolving GHG concentrations would further alter the sea surface temperature by greenhouse

254   forcing, subsequently modulating the MMV.

255   Within the 100-kyr cycle, precession-band variability (4-5 cycles), characterized by increased

256   insolation and atmospheric GHG, further heightens the positive response, leading to larger MMV

257   of subtropical rainfall. Recent transient sensitivity experiments suggests that millennial-scale

258   rainfall variability is driven primarily by meltwater and secondarily by insolation (He et al., 2021).

259   During interglacial times under the combined influence of insolation and CO_2, model simulation

260   shows that when insolation reaches the lower "threshold" value (between 358.2 and 352.1 W. m^{-2}),

261   it triggers a strong abrupt weakening of the AMOC and results in abrupt cooling transitions over

262   last 800 ka (Yin et al., 2021). Increased insolation could warm sea surface temperature and

263   accelerate freshwater input from high latitude ice sheet as well as altering GHG concentration in

264   the atmosphere (Lewkowicz and Way, 2019), which could, in turn, modulate MMV changes in the

265   low latitude monsoon regions.

266   If both millennial-scale Ca/Ti and $\delta^{18}O_{sp}$ represent subtropical rainfall amount, the

267   modulation factors should be consistent. However, MMV modulators at eccentricity, obliquity and

268   precession bands differ for loess Ca/Ti and $\delta^{18}Osp$, indicating they monitor different aspects of

269   millennial-scale monsoon circulations. Modern observations and Lagrangian trajectories of air

270   parcels in China during the summer monsoon indicate that moisture-induced precipitation doesn't

271   derive from the strongest water vapor pathways (Sun et al., 2011; Jiang et al., 2017); local water

272   vapor recycling contributes significantly to regional precipitation in East China (over 30%) and

273   North China (exceeding 55%) (Shi et al., 2020). Hence, we speculate that $\delta^{18}Osp$ MMV monitors

274   changes in the isotopic composition of rainfall, varying with changes in westerly transport paths

275   associated with North Atlantic cooling events, consistent with the MMV of $\delta^{18}Osp$ being closely

276   linked to winter insolation at 100- and 41-kyr periods and the absence of MMV modulation at

277   precession band. We further hypothesize that Ca/Ti mainly represents the MMV in local rainfall

278   amount, consistent with the MMV of tropical rainfall being more dynamically related to GHG and

279   summer insolation at precession band.

280   In recent decades, atmospheric GHG concentration is accelerating due to anthropogenic

281   contribution of fossil fuels, suggesting that extreme EASM-induced precipitation will increase as

282   well. This inference is consistent with model simulations indicating that the number of extreme

283   daily precipitation events and mean precipitation overall will increase significantly in response to

284   higher GHG concentration (Dairaku and Emori, 2006). The anthropogenic GHG-evoked warming

285   is projected to increase the lower-tropospheric water vapor content and enhance the thermal

286   contrast between land and ocean (Kitoh et al., 1997). This will give rise to a northward shift of

287   lower tropospheric monsoon circulation and an increase rainfall during the East Asian summer

288   monsoon (Vecchi and Soden, 2007). Our results indicate that factors modulating EASM

289   precipitation MMV in the past are consistent with those predicted to influence future changes in

290   monsoonal precipitation, lending further confidence in those projections.

291   **5. Conclusions**

292   Our high-resolution loess Ca/Ti record displays millennial monsoon oscillations that persist

293   over the last 650 ka. The MMV of loess Ca/Ti and speleothem $\delta^{18}O$ are modulated by different

294   orbital factors, implying that these two proxies document different climatic response of

295   millennial-scale monsoon circulation. The inferred mechanisms of how these internal and external

296   factors modulate the MMV call on dynamic linkages to variability in AMOC at both eccentricity

297   and precession bands. In recent decades, atmospheric GHG concentration is dramatically

298   increasing due to anthropogenic contribution of fossil fuels (Bousquet et al., 2006; Davis et al.,

299   2010), resulting in accelerated melting of ice-sheets in bi-polar regions (Swingedouw et al., 2008;

300   Golledge et al., 2019). Their combined effects lead to more frequent occurrences of extreme

301   rainfall (Dairaku and Emori, 2006; IPCC, 2018). Our results indicate that the MMV EASM

302   rainfall is modulated by ice volume, GHG, and insolation factors, consistent with those predicted

303   to influence future changes in monsoonal precipitation.

304

305   **CRediT authorship contribution statement**

306   Fei Guo performed data analysis and interpretation, and prepared the manuscript. Profs.

307   Steven Clemens and Youbin Sun designed this study and contributed to the interpretation and

308   writing of the manuscript. Huimin Fan assisted in the data generation and data processing. Ting

309   Wang, Yuming Liu and Xingxing Liu contributed to the fieldwork and paper discussion.

310

311   **Acknowledgments**

312   We thank Xiaojing Du for offering idea on potential model test for this paper. This work was

313 supported by grants from the Strategic Leading Research Program of Chinese Academy of Science

314 (XDB40000000) and National Natural Science Foundation of China (41525008 and 41977173).

315

Declaration of Competing Interest

317 The authors declare that they have no known competing financial interests or personal

318 relationships that could have appeared to influence the work reported in this paper.

319

References

321 Alvarez-Solas, J., Charbit, S., Ramstein, G., Paillard, D., Dumas, C., Ritz, C., and Roche, D. M.:

322 Millennial-scale oscillations in the Southern Ocean in response to atmospheric CO_2 increase,

323 Global Planet. Change, 76, 128-136, https://doi.org/10.1016/j.gloplacha.2010.12.004, 2011.

324 An, Z.: The history and variability of the East Asian paleomonsoon climate. Quat. Sci. Rev., 19,

325 171-187, https://doi.org/10.1016/S0277-3791(99)00060-8, 2000.

326 An, Z., Wu, G., Li, L., Li, J., Sun, Y., Liu, Y., Zhou, W., Cai, Y., Duan, A., Li, L., Mao, J., Cheng,

327 H., Shi, Z., Tan, L., Yan, H., Ao, H., Chang, H., and Feng, J.: Global monsoon dynamics and

328 climate change, Annu. Rev. Earth Planet., 43, 29-77,

329 https://doi.org/10.1146/annurev-earth-060313-054623, 2015.

330 Bailey, I., Bolton, C. T., DeConto, R. M., Pollard, D., Schiebel, R., and Wilson, P. A.: A low

331 threshold for North Atlantic ice rafting from "low-slung slippery" late Pliocene ice sheets,

332 Paleoceanography, 25, PA1212, https://doi.org/10.1029/2009PA001736, 2010.

333 Barker, S., and Knorr, G.: A paleo-perspective on the AMOC as a tipping element, PAGES News,

334 24, 14-15, http://orca.cardiff.ac.uk/id/eprint/95186, 2016.

335 Beck, J. W., Zhou, W., Li, C., Wu, Z., White, L., Xian, F., Kong, X., and An, Z. A 550,000-year

336 record of East Asian monsoon rainfall from [10]Be in loess. Science, 360, 877-881,

337 https://www.science.org/doi/abs/10.1126/science.aam5825, 2018.

338 Bousquet, P., Ciais, P., Miller, J. B., Dlugokencky, E. J., Hauglustaine, D. A., Prigent, C., and

339 White, J.: Contribution of anthropogenic and natural sources to atmospheric methane variability,

340   Nature, 443, 439-443, https://doi.org/10.1038/nature05132, 2006.

341 Broecker, W. S.: Massive iceberg discharges as triggers for global climate change, Nature, 372

342   421-424, https://doi.org/10.1038/372421a0, 1994.

343 Cheng, H., Edwards, L., Sinha, A., Spötl, C., Yi, L., Chen, S., Kelly, M., Kathayat, G., Wang, X. F.,

344   Li, X. L., Kong, X. G., Wang, Y. J., Ning, Y.F., and Zhang, H. W.: The Asian monsoon over the

345   past 640,000 years and ice age terminations, Nature, 534, 640-646,

346   https://doi.org/10.1038/nature18591, 2016.

347 Clark, P. U., Marshall, S. J., Clarke, G. K., Hostetler, S. W., Licciardi, J. M., and Teller, J. T.:

348   Freshwater forcing of abrupt climate change during the last glaciation, Science, 293, 283-287,

349   https://doi.org/10.1126/science.1062517, 2001.

350 Clemens, S. C., Holbourn, A., Kubota, Y., Lee, K. E., Liu, Z., Chen, G., Nelson, A., and

351   Fox-Kemper, B.: Precession-band variance missing from East Asian monsoon runoff, Nat.

352   Commun., 9, 1-12, https://doi.org/10.1038/s41467-018-05814-0, 2018.

353 Cook, E. R., Anchukaitis, K. J., Buckley, B. M., D'Arrigo, R. D., Jacoby, G. C., and Wright, W. E.:

354   Asian monsoon failure and megadrought during the last millennium, Science, 328, 486-489,

355   https://doi.org/10.1126/science.1185188, 2010.

356 Dansgaard, W., Johnsen, S. J., Clausen, H. B., Dahl-Jensen, D., Gundestrup, N. S., Hammer, C. U.,

357   Hvidberg, C. S., Steffensen, J. P., Sveinbjörnsdottir, A. E., Jouzel, J., and Bond, G.: Evidence

358   for general instability of past climate from a 250-kyr ice-core record. Nature, 364, 218-220,

359   https://doi.org/10.1038/364218a0, 1993.

360 Dairaku, K., and Emori, S.: Dynamic and thermodynamic influences on intensified daily rainfall

361   during the Asian summer monsoon under doubled atmospheric CO_2 conditions, Geophys. Res.

362   Lett., 33, L01704, https://doi.org/10.1029/2005GL024754, 2006.

363 Davis, S. J., Caldeira, K., and Matthews, H. D.: Future CO_2 emissions and climate change from

364   existing energy infrastructure, Science, 329, 1330-1333,

365   https://doi.org/10.1126/science.1188566, 2010.

366 Golledge, N. R., Keller, E. D., Gomez, N., Naughten, K. A., Bernales, J., Trusel, L. D., and

367   Edwards, T. L.: Global environmental consequences of twenty-first-century ice-sheet melt,

368   Nature, 566, 65-72, https://doi.org/10.1038/s41586-019-0889-9, 2019.

Grinsted, A., Moore, J. C., and Jevrejeva, S.: Application of the cross wavelet transform and wavelet coherence to geophysical time series, Nonlinear Proc. Geoph., 11, 561-566, https://doi.org/10.5194/npg-11-561-2004, 2004.

Guo, F., Clemens, S. C., Wang, T., Wang, Y., Liu, Y., Wu, F., Jin, Z., and Sun, Y.: Monsoon variations inferred from high-resolution geochemical records of the Linxia loess/paleosol sequence, western Chinese Loess Plateau, Catena, 198, 105019, https://doi.org/10.1016/j.catena.2020.105019, 2021.

Guo, Z., Liu, T., Guiot, J., Wu, N., Lü, H., Han, J., and Gu, Z.: High frequency pulses of East Asian monsoon climate in the last two glaciations: link with the North Atlantic. Clim. Dynam, 12, 701-709, https://doi.org/10.1007/s003820050137, 1996.

He, C., Liu, Z., Otto-Bliesner, B. L., Brady, E. C., Zhu, C., Tomas, R., Clark, P. U., Zhu, J., Jahn, A., Gu, S., and Zhang, J., Nusbaumer, J., Noone, D., Cheng, H., Wang, Y., Yan, M., and Bao, Y.: Hydroclimate footprint of pan-Asian monsoon water isotope during the last deglaciation, Sci. Adv., 7, eabe2611, https://doi.org/10.1126/sciadv.abe2611, 2021.

Heinrich, H.: Origin and consequences of cyclic ice rafting in the northeast Atlantic Ocean during the past 130,000 years, Quat. Res., 29, 142-152, https://doi.org/10.1016/0033-5894(88)90057-9, 1988.

Hemming, S. R.: Heinrich events: Massive late Pleistocene detritus layers of the North Atlantic and their global climate imprint, Rev. Geophys., 42, RG1005, https://doi.org/10.1029/2003RG000128, 2004.

Hoegh-Guldberg, O., Jacob, D., and Bindi, M., et al.: Impacts of 1.5 C global warming on natural and human systems. Global warming of 1.5 C, An IPCC Special Report. IPCC Secretariat, 175-311, http://hdl.handle.net/10138/311749, 2018.

Huang, R., Chen, J., and Huang, G.: Characteristics and variations of the East Asian monsoon system and its impacts on climate disasters in China, Adv. Atmos. Sci., 24, 993-1023, https://doi.org/10.1007/s00376-007-0993-x, 2007.

Jiang, Z., Jiang, S., Shi, Y., Liu, Z., Li, W., and Li, L.: Impact of moisture source variation on decadal-scale changes of precipitation in North China from 1951 to 2010, Geophys. Res. Atmos., 122, 600-613, https://doi.org/10.1002/2016JD025795, 2017.

398   Kitoh, A., Yukimoto, S., Noda, A., and Motoi, T.: Simulated changes in the Asian summer

399   monsoon at times of increased atmospheric CO_2, J.Meteorol. Soc. JPN. Ser. II, 75, 1019-1031,

400   https://doi.org/10.2151/jmsj1965.75.6_1019, 1997.

401   Lai, Z. P., and Wintle, A. G.: Locating the boundary between the Pleistocene and the Holocene in

402   Chinese   loess   using   luminescence,   Holocene   16,   893-899,

403   https://doi.org/10.1191/0959683606hol980rr, 2006.

404   Lewkowicz, A. G., and Way, R. G.: Extremes of summer climate trigger thousands of thermokarst

405   landslides   in   a   High   Arctic   environment,   Nat.   Commun.,   10,   1-11,

406   https://doi.org/10.1038/s41467-019-09314-7, 2019.

407   Lisiecki, L. E., and Raymo, M. E.: A Pliocene-Pleistocene stack of 57 globally distributed benthic

408        $\delta^{18}O$ records, Paleoceanography, 20, PA1003, https://doi.org/10.1029/2004PA001071, 2005.

409   Liu, J., Wang, B., Cane, M. A., Yim, S. Y., and Lee, J. Y.: Divergent global precipitation changes

410   induced   by   natural   versus   anthropogenic   forcing,   Nature,   493,   656-659,

411   https://doi.org/10.1038/nature11784, 2013.

412   Lo, L., Chang, S. P., Wei, K. Y., Lee, S. Y., Ou, T. H., and Chen, Y. C., et al.: Nonlinear climatic

413   sensitivity to greenhouse gases over past 4 glacial/interglacial cycles, Sci. Rep., 7, 1-7,

414   https://doi.org/10.1038/s41598-017-04031-x, 2017.

415   McManus, J. F., Oppo, D. W., and Cullen, J. L.: A 0.5-million-year record of millennial-scale

416   climate   variability   in   the   North   Atlantic,   Science,   283,   971-975,

417   https://doi.org/10.1126/science.283.5404.971, 1999.

418   Naafs, B. D. A., Hefter, J., and Stein, R.: Millennial-scale ice rafting events and Hudson Strait

419   Heinrich (-like) Events during the late Pliocene and Pleistocene: a review, Quat. Sci. Rev., 80,

420   1-28, https://doi.org/10.1016/j.quascirev.2013.08.014, 2013.

421   Porter, S. C., and An Z. S.: Correlation between climate events in the North Atlantic and China

422   during the last glaciation, Nature, 375, 305-308, https://doi.org/10.1038/375305a0, 1995.

423   Ramaswamy, V. et al.: Radiative forcing of climate change in Climate Change 2001: The

424   Scientific   Basis,   Cambridge   University   Press,   349-416,

425   https://csl.noaa.gov/assessments/ozone/1991/chapters/chapter7.pdf, 2001.

426   Shi, Y., Jiang, Z., Liu, Z., and Li, L.: A Lagrangian analysis of water vapor sources and pathways

427   for precipitation in East China in different stages of the East Asian summer monsoon, J. Clim.,

428   33, 977-992, https://doi.org/10.1175/JCLI-D-19-0089.1, 2020.

429   Sun, B., Zhu, Y., and Wang, H.: The recent interdecadal and interannual variation of water vapor

430   transport over eastern China, Adv. Atmos. Sci., 28, 1039-1048,

431   https://doi.org/10.1007/s00376-010-0093-1, 2011.

432   Sun, Y., Clemens, S. C., An, Z., and Yu, Z.: Astronomical timescale and palaeoclimatic implication

433   of stacked 3.6-Myr monsoon records from the Chinese Loess Plateau, Quat. Sci. Rev., 25, 33-48.

434   https://doi.org/10.1016/j.quascirev.2005.07.005, 2006.

435   Sun, Y., Clemens, S., Guo, F., Liu, X., Wang, Y., Yan, Y., and Liang, L.: High-sedimentation-rate

436   loess records: A new window into understanding orbital-and millennial-scale monsoon

437   variability, Earth-Sci. Rev., 103731, https://doi.org/10.1016/j.earscirev.2021.103731, 2021a.

438   Sun, Y., Clemens, S. C., Morrill, C., Lin, X., Wang, X., and An, Z.: Influence of Atlantic

439   meridional overturning circulation on the East Asian winter monsoon, Nat. Geosci., 5, 46-49,

440   https://doi.org/10.1038/ngeo1326, 2012.

441   Sun, Y., McManus, J. F., Clemens, S. C., Zhang, X., Vogel, H., Hodell, D. A., Guo, F., Wang, T.,

442   Liu, X., and An, Z.: Persistent orbital influence on millennial climate variability through the

443   Pleistocene, Nat. Geosci., 14, 812-818, https://doi.org/10.1038/s41561-021-00794-1, 2021b.

444   Swingedouw, D., Fichefet, T., Huybrechts, P., Goosse, H., Driesschaert, E., and Loutre, M. F.:

445   Antarctic ice-sheet melting provides negative feedbacks on future climate warming, Geophys.

446   Res. Lett., 35, https://doi.org/10.1029/2008GL034410, 2008.

447   Thirumalai, K., Clemens, S. C., and Partin, J. W.: Methane, Monsoons, and Modulation of

448   Millennial-Scale Climate, Geophys. Res. Lett., 47, e2020GL087613,

449   https://doi.org/10.1029/2020GL087613, 2020.

450   Vecchi, G. A., and Soden, B. J.: Global warming and the weakening of the tropical circulation, J.

451   Clim., 20, 4316-4340, https://doi.org/10.1175/JCLI4258.1, 2007.

452   VanderPlas, J. T.: Understanding the lomb-scargle periodogram, The Astrophysical Journal

453   Supplement Series, 236, 16, https://doi.org/10.3847/1538-4365/aab766, 2018.

454   Wang, Y., Cheng, H., Edwards, R. L., Kong, X., Shao, X., Chen, S., and An, Z. Millennial-and

455   orbital-scale changes in the East Asian monsoon over the past 224,000 years, Nature, 451,

456   1090-1093, https://doi.org/10.1038/nature06692, 2008.

457   Yin, Q. Z., Wu, Z. P., Berger, A., Goosse, H., Hodell, D.: Insolation triggered abrupt weakening of

458   Atlantic circulation at the end of interglacials, Science, 373, 1035-1040,

459   https://doi.org/10.1126/science.abg1737, 2021.

460   Zhang, H., Griffiths, M. L., Chiang, J.C.H., Kong, W., Wu, S., Atwood, A., Huang, J., Cheng, H.,

461   Ning, Y., and Xie, S.: East Asian hydroclimate modulated by the position of the westerlies

462   during Termination I, Science, 362, 580-583, https://doi.org/10.1126/science.aat9393, 2018.

463   Zhang, X., Knorr, G., Lohmann, G., and Barker, S.: Abrupt North Atlantic circulation changes in

464   response to gradual CO_2 forcing in a glacial climate state, Nat. Geosci., 10, 518-523,

465   https://doi.org/10.1038/ngeo2974, 2017.

466   Zhang, X., Lohmann, G., Knorr, G., and Purcell, C.: Abrupt glacial climate shifts controlled by ice

467   sheet changes, Nature, 512, 290-294, https://doi.org/10.1038/nature13592, 2014.

468   Zhang, Z., Li, G., Cai, Y., Cheng, X., Sun, Y., Zhao, J., Shu, P., Ma, L., and An, Z. Millennial‐

469   Scale Monsoon Variability Modulated by Low‐Latitude Insolation During the Last Glaciation.

470   Geophys. Res. Lett., 49, e2021GL096773, https://doi.org/10.1029/2021GL096773, 2022.

471
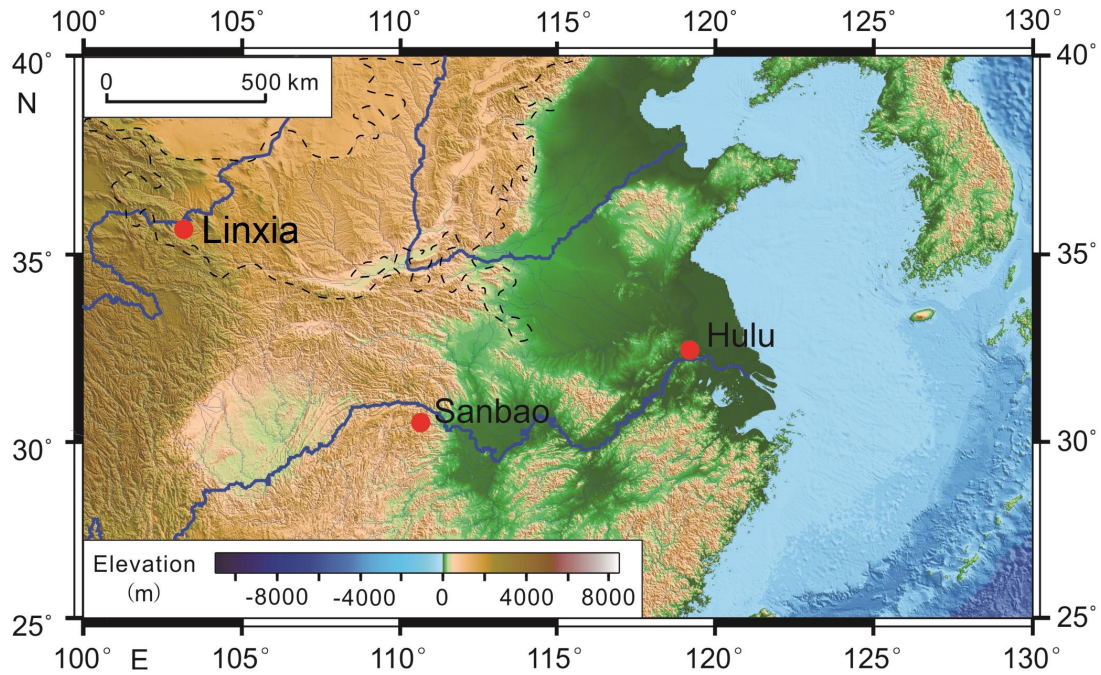
472

473   **Figure. 1** The location of the Linxia loess profile and Hulu-Sanbao cave records. The Linxia

474   profile, located on the edge of convergence zone of alpine Qinghai-Tibet Plateau, northwest arid

475   and the southeast monsoon area, is very sensitive to the migration of desert regions and monsoonal

476   rainfall. Sanbao-Hulu cave is located in monsoon-influenced Yangtze River Valley, sensitive to the

477   monsoon-induced precipitation changes. Black dashed line represents the scope of Chinese Loess

478   Plateau. The base map is drawn using GMT software, and the elevation data is from

479   http://www.ngdc.noaa.gov/mgg/global/global.html.

480

481
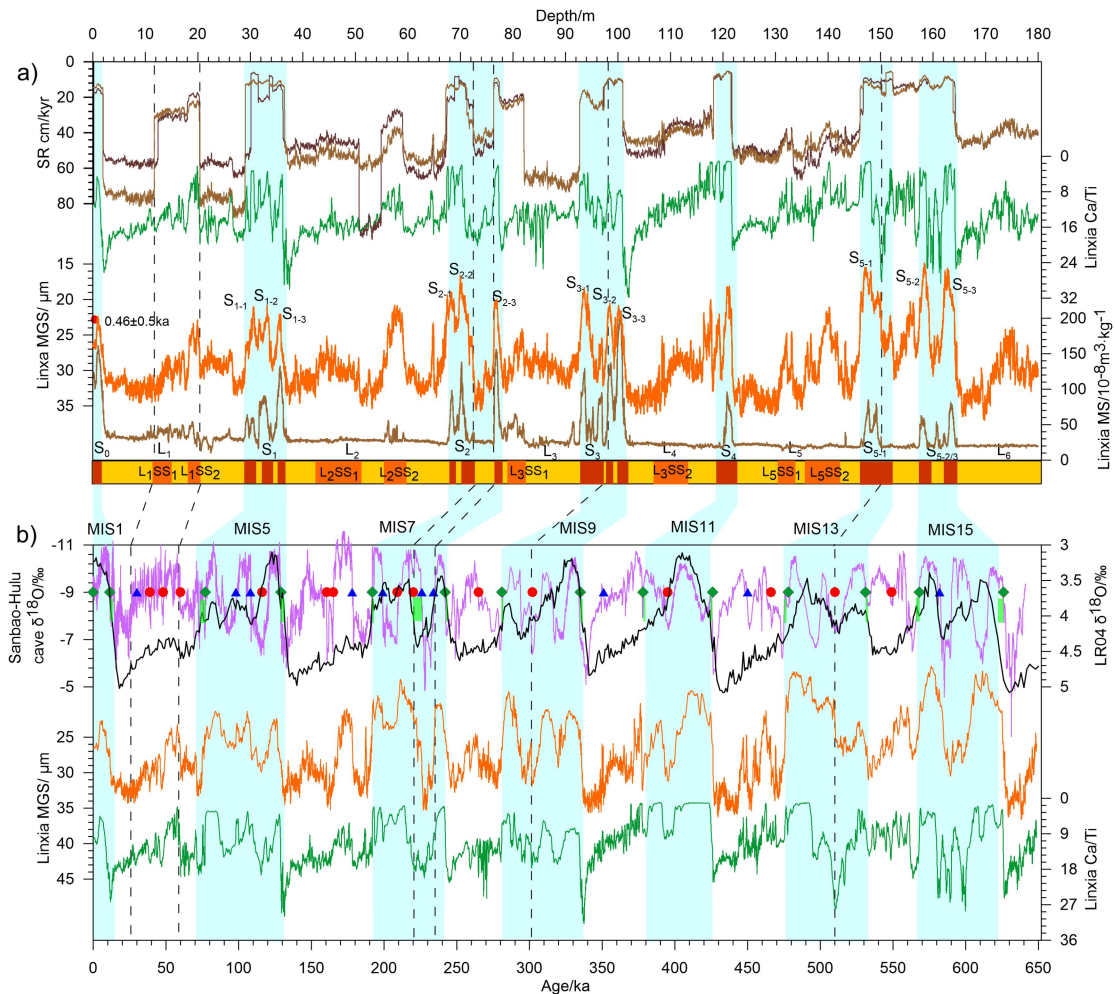
Figure 2 a) Strata and down-core variations of mean grain size (MGS), magnetic susceptibility

(MS), Ca/Ti and sedimentation rate against depth (brown in benthic δ^{18}O age model and dark

brown in speleothem δ^{18}O age model). Brown red, orange and yellow rectangles represent

palaeosol layers and weakly pedogenic palaeosols, respectively. The timing of dash lines and

glacial-interglacial transitions are control points of benthic δ^{18}O chronology; b) Variations of MGS,

Ca/Ti over last 650 ka and age model of Linxia loess section. Comparison of MGS and Ca/Ti in

Linxia section with Sanbao-Hulu (Cheng et al., 2009, 2016) and benthic δ^{18}O stack (Lisiecki and

Raymo, 2005). The dark brown squares, blue triangles and red dots represent the first

(glacial-interglacial transition), second (precession cycles) and third (millennial-scale events) class

age control points at the corresponding position of cave record, respectively (Sun et al., 2021a).

Light blue bands denote the interglacial times. The short green rectangles represent the age

differences between the two age models.

494
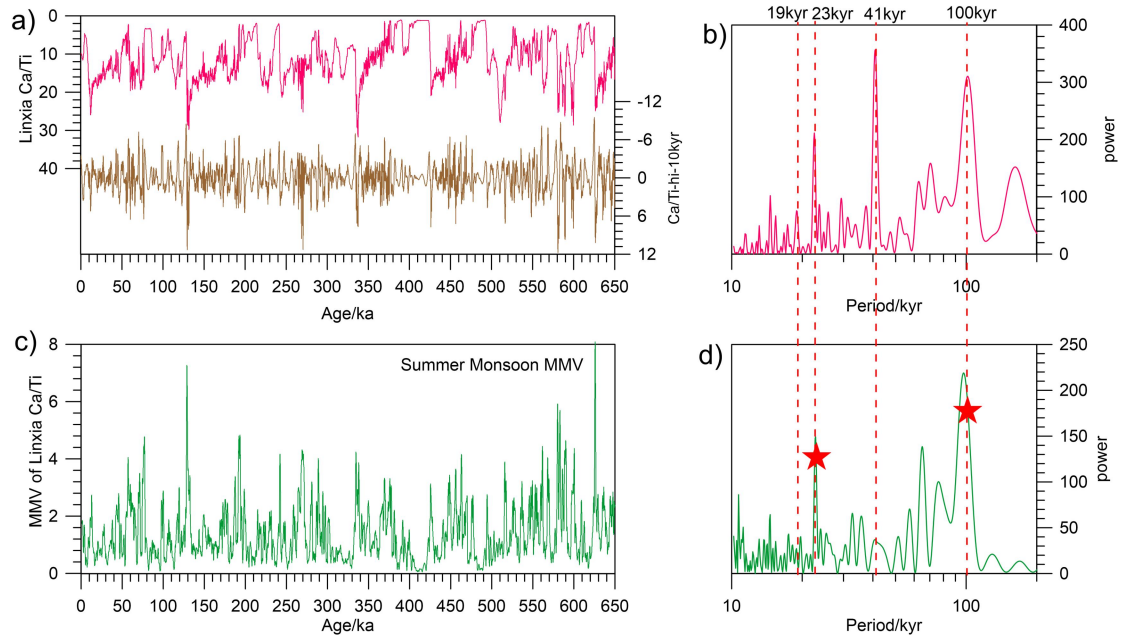
Figure. 3 Raw datasets, millennial-scale components (10-kyr high pass filtering signals) and MMV of the Linxia loess Ca/Ti record over the past 650 ka with their corresponding spectra. The orbital bands are marked with red dashed lines (eccentricity: 100-kyr, obliquity: 41-kyr, precession: 23-kyr and 19-kyr). Clear eccentricity, obliquity and precession variance as well as persistent millennial-scale components are observed for loess Ca/Ti and MMV.
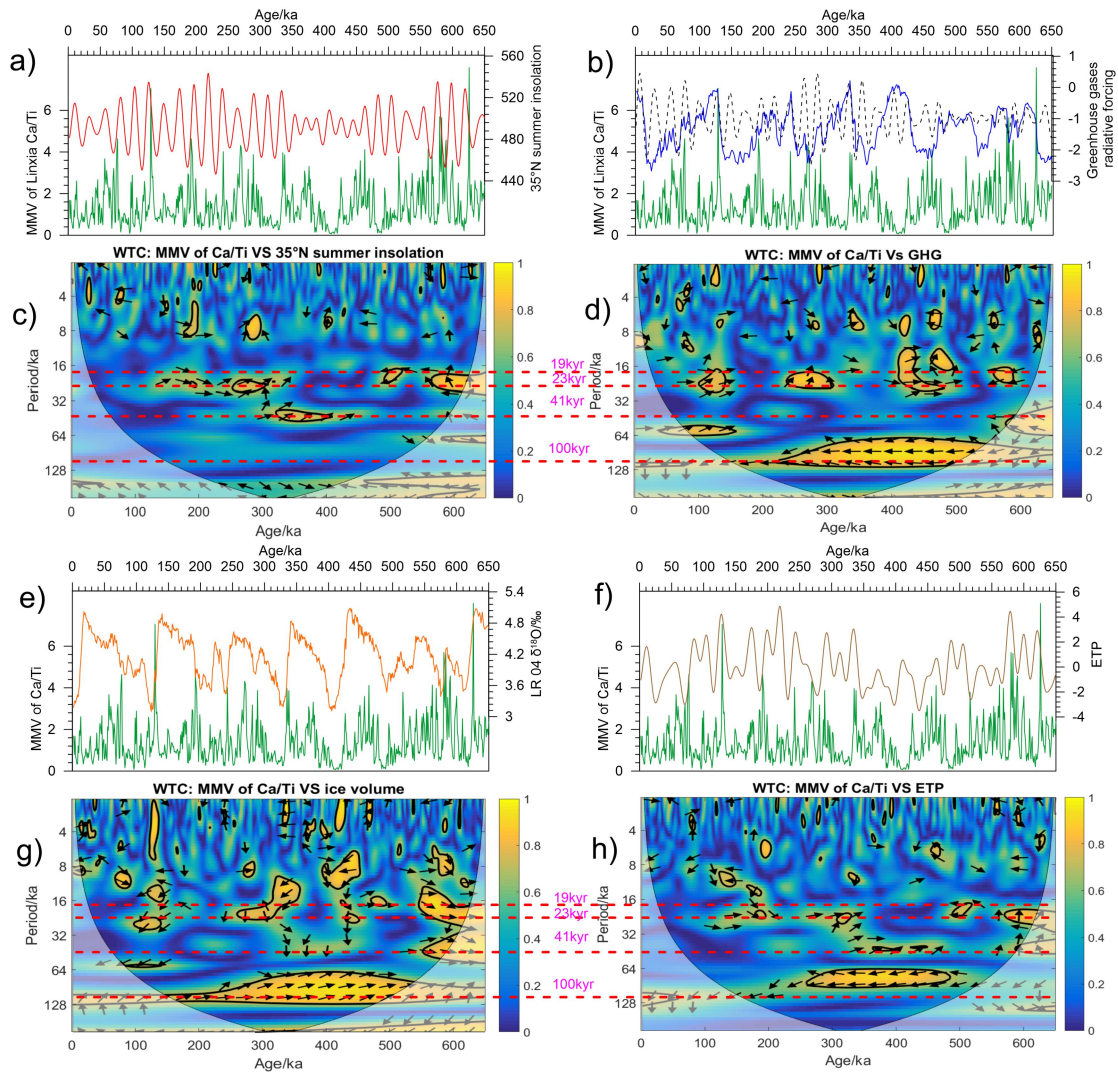
Figure. 4 Comparison of a) 35°N summer insolation forcing, b) GHG radiative forcing (black dashed line denotes the precession band-pass filtering results of ΔRF$_{GHG}$) and e) ice volume and f) ETP for MMV of Linxia loess Ca/Ti; Wavelet coherence between c) 35°N summer insolation, d) GHG radiative forcing, g) ice volume, h) ETP and MMV of loess Ca/Ti over the past 650 ka. The orbital bands are marked with red dashed lines. The orange color indicates strong correlation for the two time series. The black lines plot coefficients of determination greater than 0.76. The black arrows represent the phase relationship with rightward, upward and downward arrows indicating in-phase, leading and lagging phase, respectively. Strong eccentricity, weak obliquity and precession band ice volume modulation are observed for MMV of loess Ca/Ti. Strong eccentricity and precession band GHG modulation as well as weak summer insolation forcing are detected for MMV of loess Ca/Ti.